Supporting Information

Organic-Inorganic Hybrid Co-Containing Polyoxoniobates as Hydrogen Evolution Catalyst in Alkaline Media

Chun-Xia Chen, Shui-Lin Duan, Xiao-Yue Zhang, Rong-Zhi Sun, Ping-Wei Cai, Cai Sun* and Shou-Tian Zheng*

Fujian Provincial Key Laboratory of Advanced Inorganic Oxygenated Materials, College of Chemistry, Fuzhou University, Fuzhou, Fujian 350108, China.

E-mail: csun@fzu.edu.cn; stzheng@fzu.edu.cn

CONTENTS

1. Experimental section

Materials and measurements:

All chemicals used for syntheses were purchased from commercial sources, and no further purifications were conducted before their usages, except for the $K_7HNb_6O_{19}$ was synthesized based on the literature method.[1] The powder X-ray diffraction (PXRD) patterns were tested using a RIGAKU-Miniflex II diffractometer with Cu $K_\alpha$radiation (λ = 1.54056 Å) ranging from 5° to 50°. Fourier transform infrared spectroscopy (FT-IR) was detected by the Opus Vertex 70 FT-IR infrared spectrophotometer in the range of 4000-500 cm^{-1}. Thermogravimetric analysis (TGA) was performed using a NETZSCH STA 449C thermal analyzer with a heating rate of 10 °C/min from 30 °C to 800 °C in a dynamic argon atmosphere. The Ultraviolet-visible (UV-vis) spectra was measured on a SHIMADZU UV-2600 UV-visible spectrophotometer ranging from 200 to 800 nm by using the $BaSO_4$ as the blank. X-ray photoelectron spectroscopy (XPS) was performed in a ThermoFisher ESCALAB250 X-ray photoelectron spectrometer (powered at 150 W) using Al K_α radiation (λ = 8.357 Å). Scanning electron microscopy (SEM) and transmission elec-tron microscopy (TEM) was detected by Zeiss Sigma 300 Thermal Field Emission Scanning Electron Microscope. High-resolution TEM (HRTEM) together with its element mapping was carried out on the TEM (FEI Talos F200S G2) to further understand the microstructure details.

Synthesis of $[Co(en)_3]_3[Ti_2Nb_8O_{28}](OH)\cdot 11H_2O$ (Co_3-Ti_2Nb_8):

A mixture of $K_7H[Nb_6O_{19}]\cdot 13H_2O$ (0.66 g, 0.486 mmol), $Co(Ac)_2\cdot 4H_2O$ (0.150 g, 0.612 mmol), K_2TiF_6 (0.156 g, 0.650 mmol), $Li_2B_4O_7$ (0.063 g, 0.371 mmol) and $NaHCO_3$ (0.176 g, 2.091 mmol) was added into 8 mL distilled water. In addition, 0.10 mL en (en = ethylenediamine) were added into the solution, stirred for 1 hour, and then transferred to a glass bottle (20 mL). It was kept at 100 °C for 3 days, and cooled to room temperature. The long yellow strip crystals **Co_3-Ti_2Nb_8** were obtained by further washing with distilled water and drying completely. Yield: 100 mg (10.5 %, based on $K_7H[Nb_6O_{19}]\cdot 13H_2O$).

Synthesis of $[K(H_2O)_2]_2[Co(en)_3]_2[Ti_2Nb_8O_{28}]\cdot 8H_2O$ (Co_2-Ti_2Nb_8):

A mixture of $K_7H[Nb_6O_{19}]\cdot 13H_2O$ (0.678 g, 0.495 mmol), $Co(Ac)_2\cdot 4H_2O$ (0.151 g, 0.607 mmol), $K_2Ti(C_2O_4)\cdot 4H_2O$ (0.210 g, 0.594 mmol), $Li_2B_4O_7$ (0.075 g, 0.445 mmol) and $NaHCO_3$ (0.170 g, 2.022 mmol) was added into 8 mL distilled water. In addition, 0.10 mL en (en = ethylenediamine) were added into the solution, stirred for 1 hour, and then transferred to a glass bottle (20 mL). It was kept at 100 °C for 3 days, and cooled to room temperature. The yellow square crystals **Co_2-Ti_2Nb_8** were obtained by further washing with distilled water and drying completely. Yield: 120 mg (13.2 %, based on $K_7H[Nb_6O_{19}]\cdot 13H_2O$).

Synthesis of $[Cu(en)_2][Cu(en)_2(H_2O)_2]_3[Ti_2Nb_8O_{28}]\cdot 8H_2O$ (Cu_4-Ti_2Nb_8):

The compound **Cu_4-Ti_2Nb_8** was synthesized based on the literature method.[2] $K_7H[Nb_6O_{19}]\cdot 13H_2O$ (0.10 g), $Cu(NO_3)_2\cdot 3H_2O$ (0.10 g), titanium isopropoxide (0.3 ml) were mixed in water (8 ml). Then five drops of en were added to adjust the pH value of mixture to 11.5-12.2. The mixture was transferred into a 23ml capacity PTFE-lined autoclave and heated at 140 °C for 3 days. After slow cooling to room temperature, purple block-like crystals for X-ray crystallography were obtained, washed with distilled water and then air-dried. Yield: 115 mg (56 %, based on $K_7H[Nb_6O_{19}]\cdot 13H_2O$).

Single-crystal X-ray diffraction:

Single-crystal X-ray diffraction data of **Co_3-Ti_2Nb_8** and **Co_2-Ti_2Nb_8** were collected on the Bruker APEX-II CCD area diffractometer, using MoK_α radiation with λ = 0.71073 Å, under nitrogen atmosphere, and at 170 K. The empirical absorption correction was based on equivalent reflections. The crystal structures were solved by the direct method and refined by the full-matrix least-squares method on F^2, according to the SHELX and Olex2.[3, 4] All non-hydrogen atoms were refined anisotropically. The contribution of disordered solvent molecules to the overall intensity data of structures was treated using the SQUEEZE method in PLATON.[5] Crystallographic data for the

structures reported have been deposited in the Cambridge Crystallographic Data Centre. The entries of CCDC-2389171 and CCDC-2389169 contain the supplementary crystallographic data for **Co_3-Ti_2Nb_8** and **Co_2-Ti_2Nb_8**. These data can be obtained free of charge at http://www.ccdc.cam.ac.uk/conts/retrieving.html. The selected crystal parameters, data collection, and refinements are summarized in Table S1.

Disorder treatment details for $[Co(en)_3]_3[Ti_2Nb_8O_{28}](OH)\cdot 11H_2O$:

The en ligands coordinated to Co1 and Co3 were disordered over two sites (C1~C6, N1~N6 vs. C1A~C6A, N1A~N6A and C7~C12, N7~N12 vs. C7A~C12A, N7A~N12A) with occupancies of 0.533:0.467 and 0.803:0.197, respectively. Two Co(en)3 species (Co2 and Co4) across symmetry element were modelled as special disorder with occupancy of 0.5. The geometry and atomic displacement parameters were restrained by SHELXL SAME, DFIX, ISOR and SIMU instructions respectively to make sure the disorder components chemically reasonable and refinement stable.

The preparation of the working electrode：

For the preparation of the working electrode, 5 mg of catalyst was dispersed in a mixed solution containing 30 μL of Nafion solution (10%, DuPont, Wilmington, Delaware, USA), and 300 μL of water/isopropanol (v/v = 1:1). Then, the suspension was ultrasonicated for 30 minutes to form a homogeneous ink. The carbon cloth (CC) was first degreased by sonication in acetone and carefully washed with 0.5 M HCl in an ultrasonic bath for 20 min to remove the surface oxidation layer. Finally, apply 66 μL of catalyst ink in a uniform drop onto a CC with an area of 0.5 × 0.4 cm^2 and controlled catalyst loading of 5 mg cm^{-2}.

Electrochemical HER measurements:

Electrochemical measurements were performed in the standard three-electrode system of the Zennium-pro (Germany Zahner Instrument) electrochemical workstation. All the electrochemical tests were carried out at room temperature. Graphite rod and Hg/HgO (saturated 1 M KOH solution) electrodes were employed as the counter electrode (CE) and reference electrode (RE), respectively. In this work, the catalysis of HER was performed in 1 M KOH (pH = 13.85, 25 °C). All the potentials mentioned for this work were calibrated against the reversible hydrogen electrode (RHE) according to the equation: $E_{RHE} = E_{Hg/HgO} + 0.098 + 0.0591 \times pH$. In particular, the cyclic voltammetry (CV) tests were first performed at a scan rate of 100 mV s^{-1} for 10 cycles to attain a stable state. Then, linear sweep voltammetry (LSV) curves of HER were recorded at a scan rate of 10 mV s^{-1} over a potential range of -0.9 to -2 V. The Tafel plots were graphed using the Tafel equation, $\eta = b(\log|j|) + a$, in which b is the Tafel slope, and j is the current density. For evaluating the electrochemically active surface area (ECSA), CV was performed between -0.8 and -0.9 V at scan rates from 20 to 100 mV s^{-1}. The C_{dl} values were estimated by plotting $\Delta j = (j_a - j_c)*0.5$ at -0.85 V against the scan rates, where j_a and j_c are the anode and cathode current densities, respectively. ECSA was obtained according to the following formula, ECSA = C_{dl} / C*, where C_{dl} represents the double-layer capacitance and C* (40 μF cm^{-2}) is the specific capacitance, it is feasible to calculate the active surface area of the electrode. The turnover frequency (TOF) values were calculated from the activity of the catalysts per active site following the equation: $TOF = j \times A_{geo} / (n \times F \times m_{site})$, where j is the current density at a potential, A_{geo} is the electrode area, n is the number of electrons (2 for HER), F is the Faraday constant (96485 C/mol), and m_{site} is the total number of metal sites.[27] The EIS measurements were performed with an open-circuit potential using an AC voltage of 5 mV amplitude and a frequency range of 0.01 kHz to 100 kHz. In the end, the electrode stability was tested by the chronopotentiometry method at 10 mA cm^{-2}. All experiments were performed at room temperature.

2. Additional tables

Complex	Co_3-Ti_2Nb_8	Co_2-Ti_2Nb_8
Empirical formula	$C_{18}H_{95}Co_3N_{18}Nb_8O_{40}Ti_2$	$C_{12}H_{72}Co_2K_2N_{12}Nb_8O_{40}Ti_2$
Formula weight	2219.98	2059.810
Crystal size (mm^3)	0.3 × 0.1 × 0.1	0.2 × 0.2 × 0.1
Crystal system	monoclinic	monoclinic
Space group	$P2_1/c$	$P2_1/n$
***a* (Å)**	12.1776(4)	9.882(3)
***b* (Å)**	38.7820(14)	21.468(5)
***c* (Å)**	14.7815(6)	12.867(3)
α (°)	90	90
β (°)	100.796(4)	92.361(3)
γ (°)	90	90
***V* (Å^3)**	6857.3(4)	2727.3(12)
Z	4	2
***F*(000)**	4396.0	1851.4
ρ_{calcd}(g cm^{-3})	2.150	2.508
Temperature (K)	170.0	170.0
μ(mm^{-1})	2.305	2.743
Refl. Collected	62174	11168
Independent relf.	15898	4735
Parameters	1144	373
GOF on F^2	1.089	1.065
R_1 [$I > 2\sigma$]	R_1[a] = 0.0830, wR_2[b] = 0.1942	R_1[a] = 0.0173, wR_2[b] = 0.0414
R_1(all data)	R_1[a] = 0.1069, wR_2[b] = 0.2049	R_1[a] = 0.0192, wR_2[b] = 0.0422

Table S1. Crystallographic data for Co_3-Ti_2Nb_8 and Co_2-Ti_2Nb_8.

[a]$R_1 = \sum||F_o| - |F_c||/\sum|F_o|$. [b]$wR_2 = \{\sum w(F_o^2 - F_c^2)^2/\sum w(F_o^2)^2]\}^{1/2}$

Table S2. Bond values and calculations for each atom in Co_3-Ti_2Nb_8.

Atoms code	Bond Valence	Valence state
Nb1	4.88842	5
Nb2	4.86555	5
Nb3	4.84642	5
Nb4	4.95897	5
Nb5	4.91144	5
Nb6	4.86244	5
Nb7	4.86906	5
Nb8	4.94513	5
Ti1	3.93243	4
Ti2	3.96302	4
Co1	2.70201	3
Co2	2.81466	3
Co3	2.70120	3
Co4	2.68326	3

Table S3. Bond values and calculations for each atom in Co_2-Ti_2Nb_8.

Atoms code	Bond Valence	Valence state
Nb1	4.86198	5
Nb2	4.84258	5
Nb3	4.88145	5
Nb4	4.84278	5
Ti1	3.97044	4
Co1	2.49696	3

Table S4 Selected bond lengths (Å) for Co_3-Ti_2Nb_8

Bond	Dist	Bond	Dist
Nb1-O5	1.982(8)	Co2-N2	1.93(2)
Nb1-O13	2.026(7)	Co2-N2[1]	1.93(2)
Nb1-O16	2.455(6)	Co3-N7	1.946(15)
Nb1-O21	1.768(8)	Co3-N8	1.967(17)
Nb1-O22	1.973(7)	Co3-N9	1.904(16)
Nb1-O27	2.002(8)	Co3-N10	1.990(17)
Nb2-O2	2.122(7)	Co3-N11	1.994(17)
Nb2-O5	1.938(7)	Co3-N12	2.000(18)
Nb2-O6	2.071(7)	Co4-N80	1.85(2)
Nb2-O7	1.922(7)	Co4-N80[2]	1.87(2)
Nb2-O14	1.767(8)	Co4-N34	1.94(2)
Nb2-O16	2.385(6)	Co4-N34[2]	1.94(2)
Nb3-O1	1.764(8)	Co4-N79	1.95(2)
Nb3-O2	2.086(7)	Co4-N79[2]	1.95(2)
Nb3-O6	2.080(7)	Ti1-O2	2.006(7)
Nb3-O24	1.954(8)	Ti1-O8	1.813(7)
Nb3-O26	2.400(7)	Ti1-O13	1.825(7)
Nb3-O28	1.932(8)	Ti1-O16	2.184(7)
Nb4-O8	2.019(8)	Ti1-O18	2.020(7)
Nb4-O12	1.752(8)	Ti1-O26	2.143(7)
Nb4-O19	1.970(9)	Ti2-O3	1.820(7)
Nb4-O20	1.996(8)	Ti2-O6	1.982(7)
Nb4-O24	1.987(9)	Ti2-O9	2.022(7)
Nb4-O26	2.482(7)	Ti2-O11	1.824(7)
Nb5-O3	2.035(7)	Ti2-O16	2.163(7)
Nb5-O17	2.000(8)	Ti2-O26	2.155(7)
Nb5-O19	1.975(9)	N1-C11	1.12(5)
Nb5-O25	1.745(9)	N80-C16	1.37(4)
Nb5-O26	2.477(7)	N80-C14	1.398(10)
Nb5-O28	2.002(8)	N3-C9	1.51(3)
Nb6-O4	1.755(9)	N4-C13	1.59(4)
Nb6-O9	2.097(7)	N5-C12	1.67(4)

Bond	Dist	Bond	Dist
Nb6-O17	1.939(8)	N6-C1	1.70(6)
Nb6-O18	2.093(7)	N7-C3	1.50(2)
Nb6-O20	1.935(8)	N8-C5	1.55(3)
Nb6-O26	2.412(7)	N9-C4	1.63(2)
Nb7-O9	2.098(7)	N10-C10	1.46(3)
Nb7-O15	1.918(8)	N11-C7	1.61(3)
Nb7-O16	2.421(6)	N12-C8	1.50(3)
Nb7-O18	2.116(7)	N34-C18	1.49(4)
Nb7-O23	1.761(9)	N34-C23	1.47(5)
Nb7-O27	1.926(8)	N79-C17	1.25(3)
Nb8-O7	2.010(7)	N79-C21	1.24(4)
Nb8-O10	1.745(8)	N15-C6	1.57(3)
Nb8-O11	2.019(7)	N14-C2	1.43(3)
Nb8-O15	1.987(7)	N2-C19	1.38(4)
Nb8-O16	2.452(6)	C2-C19	1.62(4)
Nb8-O22	1.984(8)	C3-C7	1.52(3)
Co1-N1	2.00(2)	C4-C5	1.53(3)
Co1-N3	1.948(13)	C6-C9	1.63(4)
Co1-N4	1.935(14)	C8-C10	1.56(3)
Co1-N5	1.949(16)	C11-C1	1.57(6)
Co1-N6	1.965(16)	C12-C13	1.56(5)
Co1-N15	1.965(12)	C16-C17[2]	1.75(4)
Co2-O33[1]	1.99(2)	C17-C21	1.91(5)
Co2-O33	1.99(2)	C18-C14[2]	1.82(5)
Co2-N14	1.96(2)	C21-C23[2]	1.66(7)
Co2-N14[1]	1.96(2)		

Table S5 Selected bond lengths (Å) for Co_2-Ti_2Nb_8

Bond	Dist	Bond	Dist
Nb1-O1	1.773(3)	Co1-N4	1.974(4)
Nb1-O3	2.006(3)	Co1-N5	1.975(4)
Nb1-O7	2.471(3)	Co1-N6	1.974(4)
Nb1-O9	1.967(3)	Ti1-O2	2.019(3)

Bond	Dist	Bond	Dist
Nb1-O10	2.039(3)	Ti1-O4	1.990(3)
Nb1-O11	1.971(3)	Ti1-O6	1.833(3)
Nb2-O21	2.096(3)	Ti1-O7	2.130(3)
Nb2-O3	1.925(3)	Ti1-O7[1]	2.141(3)
Nb2-O4	2.088(3)	Ti1-O10[1]	1.823(3)
Nb2-O7	2.392(3)	K1-O4	3.209(3)
Nb2-O8	1.930(3)	K1-O6	2.976(3)
Nb2-O13	1.778(3)	K1-O8	2.895(3)
Nb3-O5	1.967(3)	K1-O11[4]	2.951(3)
Nb3-O6	2.038(3)	K1-O14[4]	3.110(3)
Nb3-O7	2.479(3)	K1-O16[4]	2.820(4)
Nb3-O8	2.011(3)	K1-O20[3]	2.755(4)
Nb3-O9	1.969(3)	K1-O20	2.723(4)
Nb3-O12	1.766(3)	N1-C5	1.504(6)
Nb4-O2	2.114(3)	N2-C2	1.488(6)
Nb4-O4[1]	2.105(3)	N3-C4	1.493(6)
Nb4-O5	1.929(3)	N4-C3	1.499(6)
Nb4-O7	2.440(3)	N5-C6	1.511(6)
Nb4-O11	1.932(3)	N6-C1	1.491(6)
Nb4-O14	1.752(3)	C1-C4	1.525(7)
Co1-N1	1.969(4)	C2-C3	1.516(6)
Co1-N2	1.962(4)	C5-C6	1.520(7)
Co1-N3	1.970(4)		

Table S6. The comparison of HER catalytic activity of the present study with the reported systems.

Catalysts	Electrolyte	overpotential (η)@ mA/cm^2	Ref.
CoP-2ph-CMP-800	1.0 M KOH	360 mV@10	6
Co/NGC-3	0.1 M KOH	293 mV@10	7
Co_9S_8/NiS@C/GC	1.0 M KOH	280mV@10	8
Co-P-300	1.0 M KOH	280 mV@10	9
CuCo@NC	0.1 M KOH	277 mV@10	10
Co/CoP-NC	1.0 M KOH	260 mV@10	11
V_3Nb_{12}	0.1 M KOH	258.1 mV@10	12
Co/CoP-5	1.0 M KOH	253 mV@10	13
Co-PCNFs	1.0 M KOH	249 mV@10	14
$CTS_{0.2}$-rGO/NF	1.0 M KOH	233.1 mV@20	15
Co@NG	1.0 M KOH	220 mV@10	16
$Cu_{0.3}Co_{2.7}P$/NC	1.0 M KOH	220 mV@10	17
CoP/CC	1.0 M KOH	209 mV@10	18
CoS_2NTA/CC	1.0 M KOH	193 mV@10	19
$(Fe_{0.75}Co_{0.25})_5C_2$	0.1 M KOH	174 mV@10	20
$[Ti_2Nb_8O_{28}]$-{Co(en)}$_3$	**1.0 M KOH**	**172mV@10**	**This work**
CoS_2-MoS_2/CC	1.0 M KOH	147 mV@10	21
Co-Mo-S/CC	1.0 M KOH	118 mV@10	22

3. Additional figures

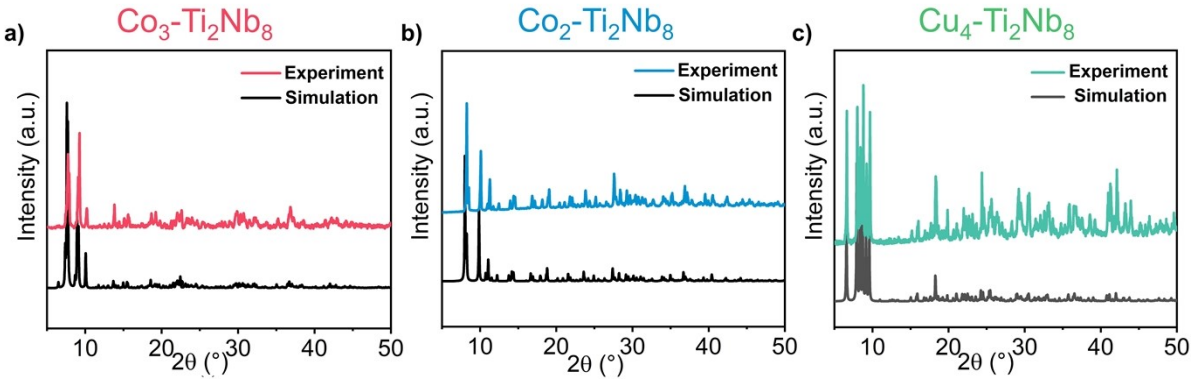

Fig. S1. Simulated and experimental PXRD patterns of a) **Co_3-Ti_2Nb_8**, b) **Co_2-Ti_2Nb_8** and c) **Cu_4-Ti_2Nb_8**.

The powder X-ray diffraction test was carried out for the three compounds of **Co_3-Ti_2Nb_8**, **Co_2-Ti_2Nb_8** and **Cu_4-Ti_2Nb_8** at room temperature (Fig. S1a, 1b, 1c). The peak positions are consistent with the simulated diffraction peak, indicating that the powder samples of the compound powder samples are pure phase.

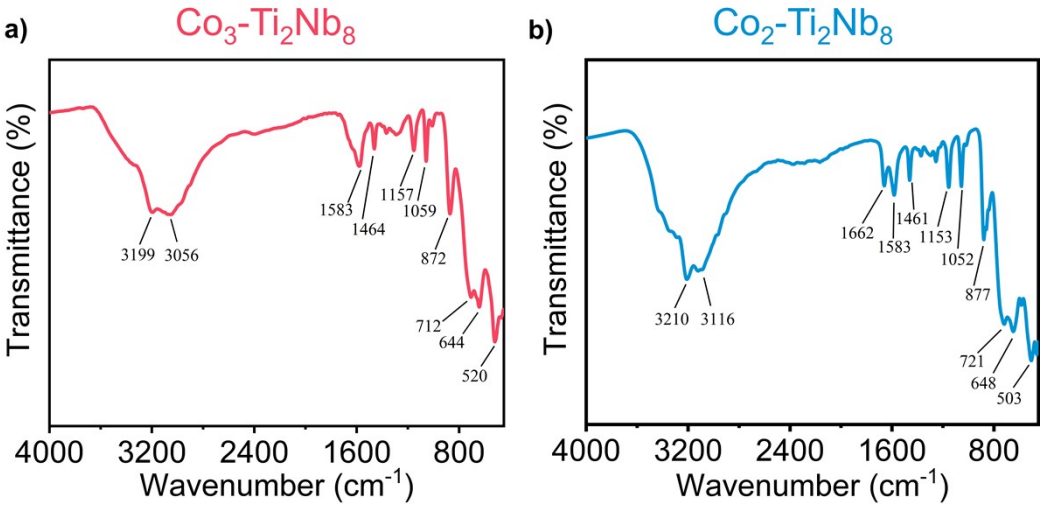

Fig. S2. IR spectrum of a) **Co_3-Ti_2Nb_8** and b) **Co_2-Ti_2Nb_8**.

Fourier transform infrared (FTIR) of **Co_3-Ti_2Nb_8** and **Co_2-Ti_2Nb_8** were tested. As shown in Fig. S2a, 2b, The IR spectrum of **Co_3-Ti_2Nb_8** is shown in Fig. S2a. The broad absorption peaks around 3200 cm^{-1} are attributed to the ν(O–H) stretching vibration of water. Peaks at 3056 cm^{-1} and 3199 cm^{-1} are attributed to the ν(C–H) and ν(N–H) stretching vibrations, while the peaks at 1583 cm^{-1}, 1464 cm^{-1} ascribe to the δ(N–H) and δ(C–H) bending vibrations. Peaks at positions 1157 cm^{-1} and 1059 cm^{-1}mainly ascribe to the ν(C-N). The absorption at 872 cm^{-1} is attributed to the ν(Nb=O_t) vibrations of **Co_3-Ti_2Nb_8**, while the peaks at 712 cm^{-1}, 644 cm^{-1} and 520 cm^{-1} belong to the ν(Nb–O_b–Nb) vibrations.

The IR spectrum of **Co_2-Ti_2Nb_8** is similar to **Co_3-Ti_2Nb_8** as shown in Fig. S2b. Peaks at 3210 cm^{-1}ascribe to the ν(O–H) and ν(N–H). Peaks at 3116 cm^{-1} are attributed to the ν(C–H) stretching vibrations, while the peaks at 1583 cm^{-1}, 1461 cm^{-1} ascribe to the δ(N–H) and δ(C–H) bending vibrations. Peaks at

positions 1153 cm^{-1} and 1052 cm^{-1}mainly ascribe to the ν(C-N). The absorption at 877 cm^{-1} is attributed to the ν(Nb=O_t) vibrations, while the peaks at 721 cm^{-1}, 648 cm^{-1} and 503 cm^{-1} belong to the ν(Nb–O_b–Nb) vibrations.

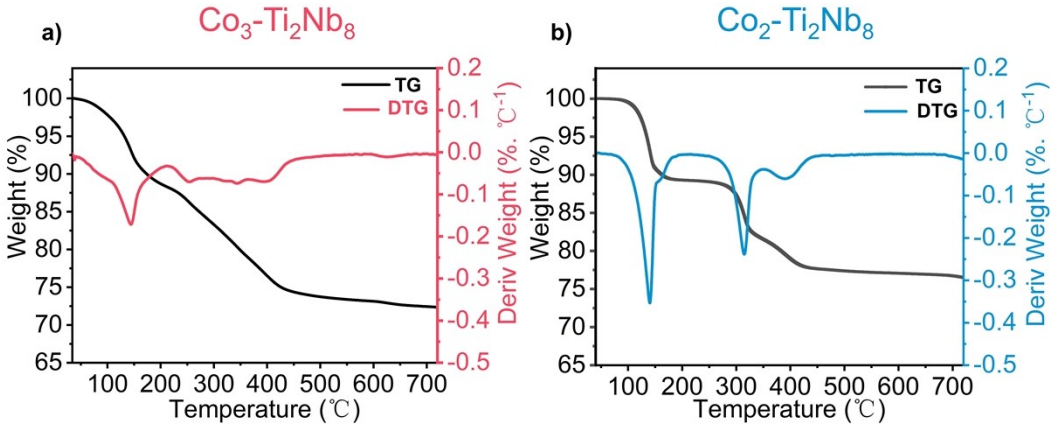

Fig. S3. TG and DTG curves of a) **Co_3-Ti_2Nb_8** and b) **Co_2-Ti_2Nb_8.**

As shown in Fig. S3, the thermogravimetric analysis of the **Co_3-Ti_2Nb_8** is shown in Fig. S3a. The first weight-loss stage within the range of 25 °C to 169.83 °C mainly ascribed to the loss of water molecules. Based on the first weight-loss of about 8.21 % for **Co_3-Ti_2Nb_8**, there are about 11 water molecules. The thermogravimetric analysis of the **Co_2-Ti_2Nb_8** is shown in Fig. S3b, the first weight-loss stage within the range of 25 °C to 170.67 °C mainly ascribed to the loss of water molecules. Based on the first weight-loss of about 10.35 % for **Co_2-Ti_2Nb_8,** corresponding to the loss of 8 free water molecules, 4 ligand water molecules.

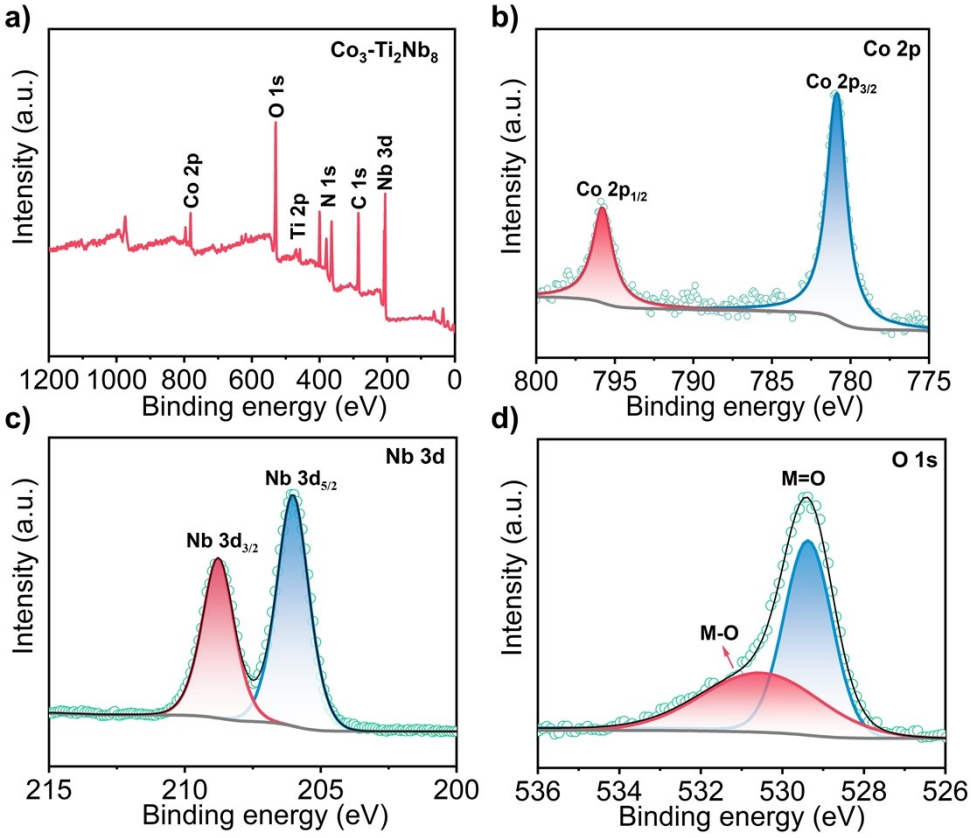

Fig. S4. XPS spectra of **Co_3-Ti_2Nb_8**. a) survey spectrum; b) XPS spectrum of Co 2p; c) XPS spectrum of Nb

3d; d) XPS spectrum of O 1s.

The XPS measured spectra of **Co_3-Ti_2Nb_8** are shown in Fig. S4. The presence of the elements Nb, Ti, Co, O, N, and C is evident as shown in Fig. S4a. The Co 2p spectrum consists of two spin-orbit bimodal peaks, and the observation that the Co $2p_{3/2}$ and Co $2p_{1/2}$ binding energies of 780.88 and 795.88 eV, respectively (Fig. S4b). These results indicate that cobalt ions exist in their highest oxidation state, i.e., Co^{3+}.[23, 24] The Nb $3d_{5/2}$ and Nb $3d_{3/2}$ peaks are attributed to the Nb 3d spectra of **Co_3-Ti_2Nb_8**, located at 206.08 and 208.78 eV, respectively (Fig. S4c). In addition, as shown in Fig. S4d, the fitted O 1s high-resolution spectra and fitted peaks correspond to the Nb-O bond (529.38 eV) and Co-O bond, (530.68 eV) respectively.[25, 26]

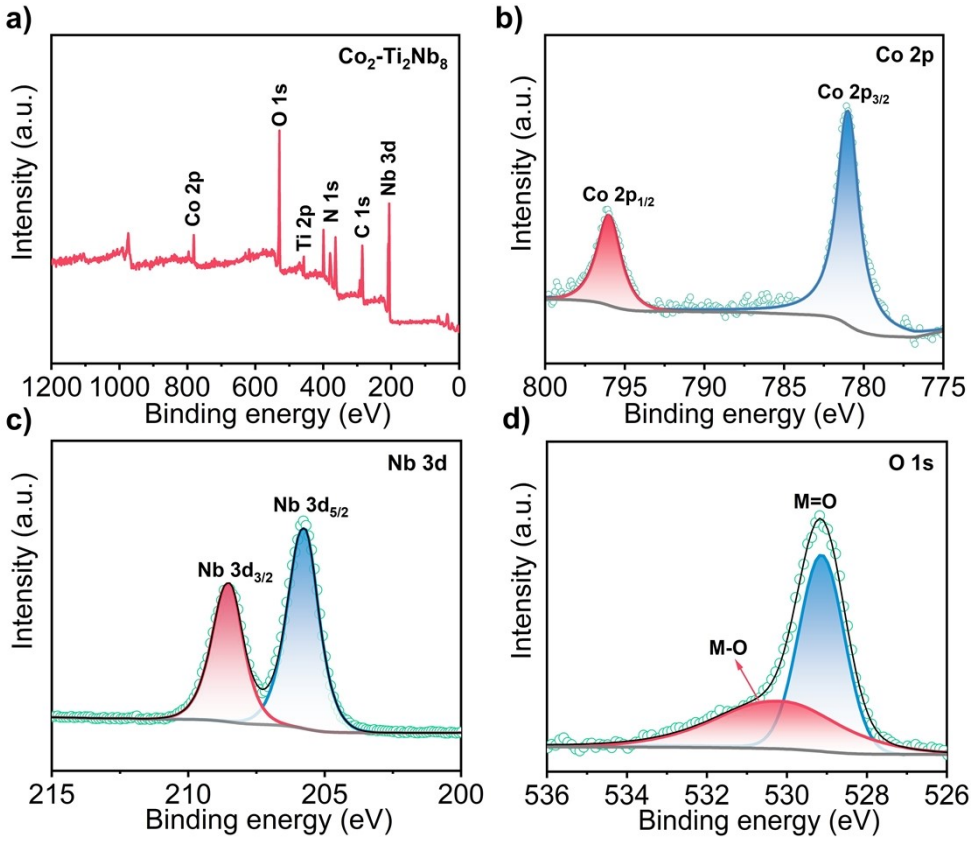

Fig. S5. XPS spectra of **Co_2-Ti_2Nb_8**. a) survey spectrum; b) XPS spectrum of Co 2p; c) XPS spectrum of Nb 3d; d) XPS spectrum of O 1s.

The XPS measured spectra of **Co_2-Ti_2Nb_8** are shown in Fig. S5. The presence of the elements Nb, Ti, Co, O, N, and C is evident as shown in Fig. S5a. The Co 2p spectrum consists of two spin-orbit bimodal peaks and two accompanying peaks, and the observation that the Co $2p_{3/2}$ and Co $2p_{1/2}$ binding energies of 780.88 and 795.78 eV, respectively (Fig. S5b). These results indicate that cobalt ions exist in their highest oxidation state, i.e., Co^{3+}[24, 25] The Nb $3d_{5/2}$ and Nb $3d_{3/2}$ peaks are attributed to the Nb 3d spectra of **Co_2-Ti_2Nb_8**, located at 205.78 and 208.58 eV, respectively (Fig. S5c). In addition, as shown in Fig. S5d, the fitted O 1s high-resolution spectra and fitted peaks correspond to the Nb-O bond (529.18 eV) and Co-O bond, (530.28 eV) respectively.

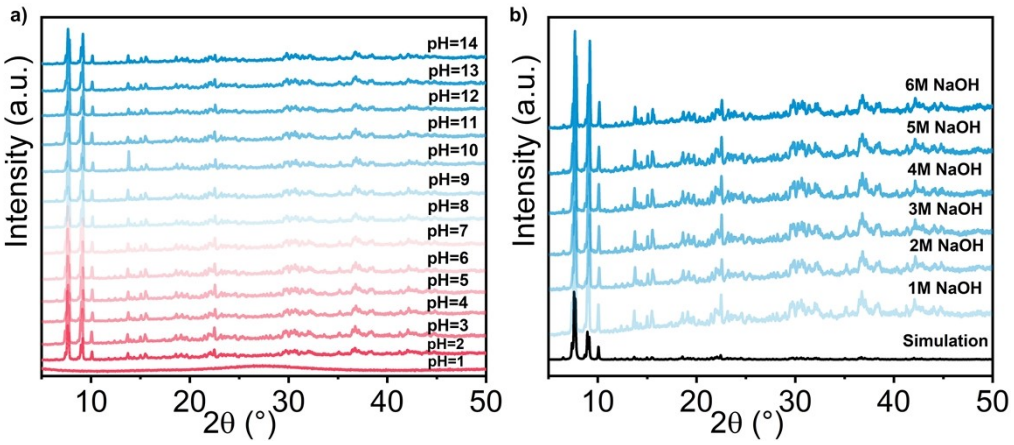

Fig. S6. Simulated and experimental PXRD patterns of **Co_3-Ti_2Nb_8** a) in pH = 1-14 KOH solutions and b) in 1-6 M NaOH solutions.

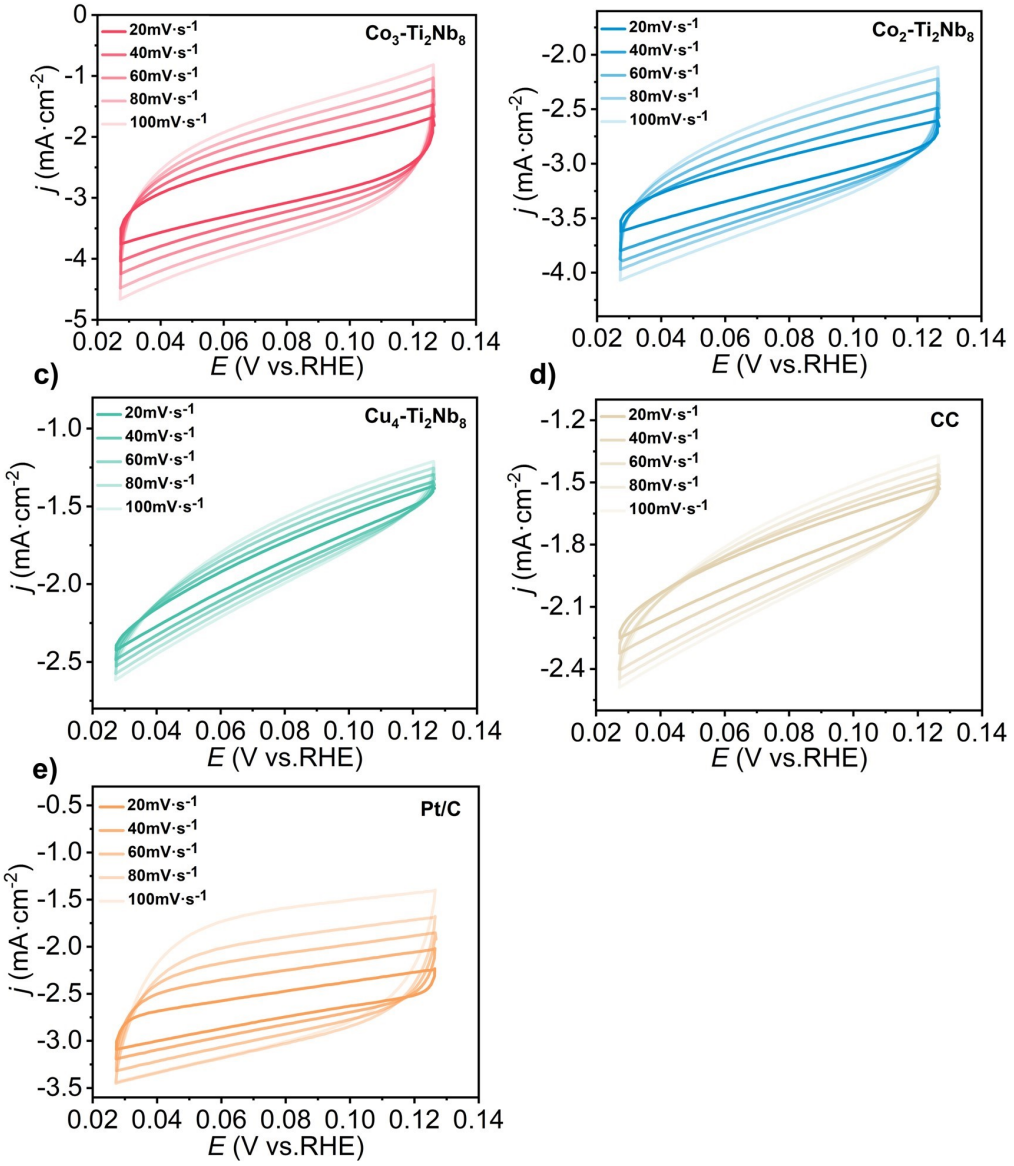

Fig. S7. CV curves for HER in 1.0 M KOH solution at a scan rate of 20, 40, 60, 80 and 100 mV s^{-1}: a) **Co_3-Ti_2Nb_8** b) **Co_2-Ti_2Nb_8**, c) **Cu_4-Ti_2Nb_8**, d) Bare **CC** e) **Pt/C**.

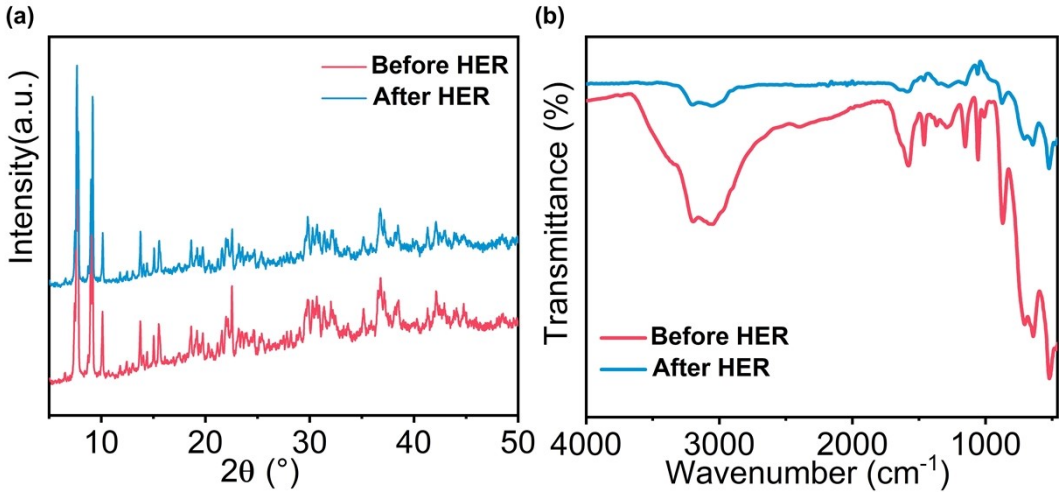

Fig. S8. a). Powder XRD patterns of **Co_3-Ti_2Nb_8** before and after 130 hours HER. b). IR spectrum of **Co_3-Ti_2Nb_8** before and after 130 hours HER.

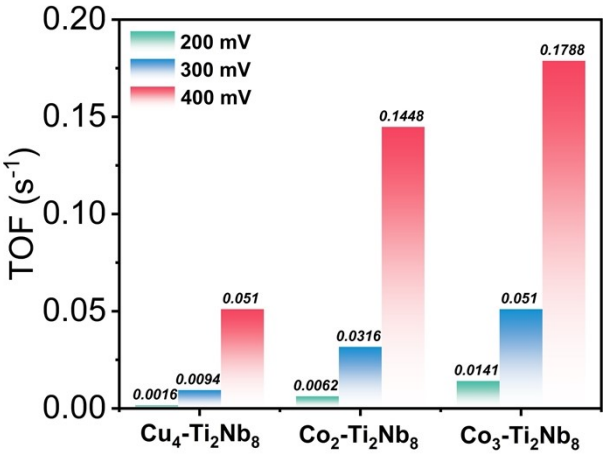

Fig. S9. a). TOF values of **Co_3-Ti_2Nb_8**, **Co_2-Ti_2Nb_8** and **Cu_4-Ti_2Nb_8**.

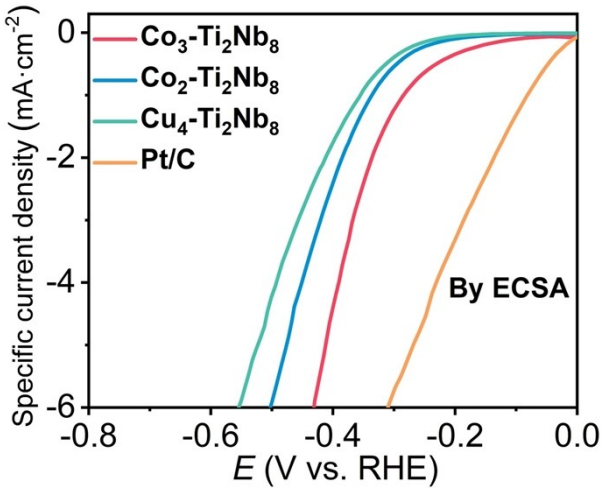

Fig. S10. LSV curves of **Co_3-Ti_2Nb_8**, **Co_2-Ti_2Nb_8**, **Cu_4-Ti_2Nb_8** and **Pt/C** normalized by ECSA.

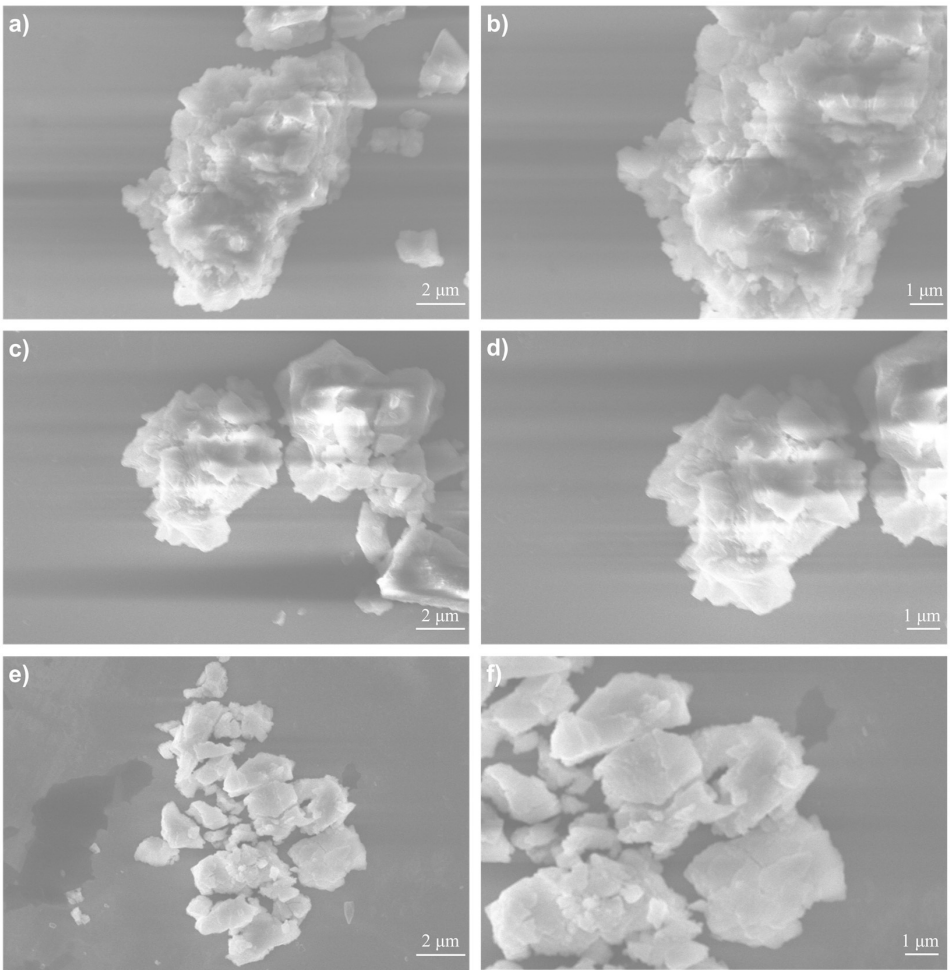

Fig. S11. Samples morphology. a), b) The FESEM images of **Co_3-Ti_2Nb_8**. Scale bars, 2 µm and 1 µm, respectively. c), d) The FESEM images of **Co_2-Ti_2Nb_8**. Scale bars, 2 µm and 1 µm, respectively. e), f) The FESEM images of **Cu_4-Ti_2Nb_8**. Scale bars, 2 µm and 1 µm, respectively.

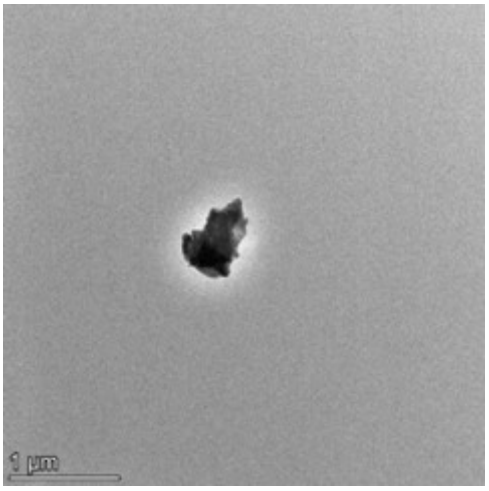

Fig. S12. TEM images of **Cu_4-Ti_2Nb_8**.

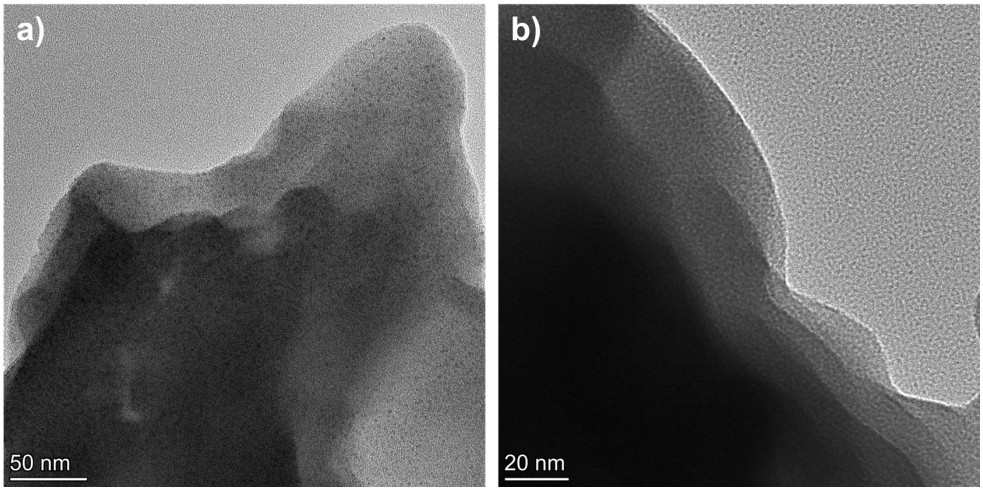

Fig. S13. a). and b). HRTEM images of **Cu_4-Ti_2Nb_8**.

4. References

1. M. FILOWITZ, R. K. C. HO, W. G. KLEMPERER, and W. SHUM, ^{17}O Nuclear Magnetic Resonance Spectroscopy of Polyoxometalates. 1. Sensitivity and Resolution, *Inorg. Chem.*, 1978, **18**, 93-103.
2. Y.-T. Zhang, P. Huang, C. Qin, L.-K. Yan, B.-Q. Song, Z.-X. Yang, K.-Z. Shao and Z.-M. Su, A novel organic–inorganic hybrid constructed from the Nyman-type dititanoniobate $[Ti_2Nb_8O_{28}]^{8-}$ and copper–organic cations, *Dalton Trans.*, 2014, **43**, 9847-9850.
3. G. M. Sheldrick, A short history of SHELX, *Acta Crystallogr., Sect. A: Found. Crystallogr.*, 2007, **64**, 112-122.
4. G. M. Sheldrick, Crystal structure refinement with SHELXL, *Acta Crystallogr., Sect. C: Struct. Chem.*, 2015, **71**, 3-8.
5. A. L. Spek, PLATONSQUEEZE: a tool for the calculation of the disordered solvent contribution to the calculated structure factors, *Acta Crystallogr., Sect. C: Struct. Chem.*, 2015, **71**, 9-18.
6. H. X. Jia, Y. C. Yao, Y. Y. Gao, D. P. Lu and P. W. Du, Pyrolyzed cobalt porphyrin-based conjugated mesoporous polymers as bifunctional catalysts for hydrogen production and oxygen evolution in water, *Chem. Commun.*, 2016, **52**, 13483-13486.
7. J. M. Li, Y. M. Kang, D. Liu, Z. Q. Lei and P. Liu, Nitrogen-Doped Graphitic Carbon-Supported Ultrafine Co Nanoparticles as an Efficient Multifunctional Electrocatalyst for HER and Rechargeable Zn–Air Batteries, *ACS Appl. Mater. Interfaces.*, 2020, **12**, 5717-5729.
8. A. S. a. D. BARFORD, Functions and Mechanisms of Redox Regulation of Cysteine-Based Phosphatases, *Antioxid. Redox Signal*, 2005, **7**, 560-577.
9. Y. Feng, X.-Y. Yu and U. Paik, Nickel cobalt phosphides quasi-hollow nanocubes as an efficient electrocatalyst for hydrogen evolution in alkaline solution, *Chem. Commun.*, 2016, **52**, 1633-1636.
10. M. Kuang, Q. Wang, P. Han and G. Zheng, Cu, Co-Embedded N-Enriched Mesoporous Carbon for Efficient Oxygen Reduction and Hydrogen Evolution Reactions, *Adv. Energy Mater.*, 2017, **7**, 1700193.
11. Y. Hao, Y. Xu, W. Liu and X. Sun, Co/CoP embedded in a hairy nitrogen-doped carbon polyhedron as an advanced tri-functional electrocatalyst, *Mater. Horiz.*, 2018, **5**, 108-115.
12. R.-Z. Sun, J.-X. Chen, S.-L. Huang, W.-T. Weng, H.-P. Wu, P.-W. Cai, Z.-H. Wen and S.-T. Zheng, Dissecting Structural Modification Effects on the Electrocatalytic Hydrogen Evolution Reaction Activity of

Atomically Precise Polyoxometalates, *CCS Chem.*, 2024, 1-23.

13. Z. H. Xue, H. Su, Q. Y. Yu, B. Zhang, H. H. Wang, X. H. Li and J. S. Chen, Janus Co/CoP Nanoparticles as Efficient Mott–Schottky Electrocatalysts for Overall Water Splitting in Wide pH Range, *Adv. Energy Mater.*, 2017, **7**, 1602355.
14. Y. Zhao, J. Zhang, K. Li, Z. Ao, C. Wang, H. Liu, K. Sun and G. Wang, Electrospun cobalt embedded porous nitrogen doped carbon nanofibers as an efficient catalyst for water splitting, *J. Mater. Chem. A*, 2016, **4**, 12818-12824.
15. M. Khademalrasool and E. Kharatzadeh, SnS-rGO heterojunction: Fabrication, characterization, and visible light-induced optoelectronic performance analysis, *J. Photochem. Photobiol., A.*, 2023, **443**, 114878.
16. M. Zeng, Y. Liu, F. Zhao, K. Nie, N. Han, X. Wang, W. Huang, X. Song, J. Zhong and Y. Li, Metallic Cobalt Nanoparticles Encapsulated in Nitrogen-Enriched Graphene Shells: Its Bifunctional Electrocatalysis and Application in Zinc–Air Batteries, *Adv. Funct. Mater.*, 2016, **26**, 4397-4404.
17. J. H. Song, C. Z. Zhu, B. Z. Xu, S. Fu, M. H. Engelhard, R. Ye, D. Du, S. P. Beckman and Y. Lin, Bimetallic Cobalt-Based Phosphide Zeolitic Imidazolate Framework: CoP_x Phase-Dependent Electrical Conductivity and Hydrogen Atom Adsorption Energy for Efficient Overall Water Splitting, *Adv. Energy Mater.*, 2016, **7**, 1601555.
18. J. Tian, Q. Liu, A. M. Asiri and X. Sun, Self-Supported Nanoporous Cobalt Phosphide Nanowire Arrays: An Efficient 3D Hydrogen-Evolving Cathode over the Wide Range of pH 0–14, *J. Am. Chem. Soc.*, 2014, **136**, 7587-7590.
19. C. Guan, X. M. Liu, A. M. Elshahawy, H. Zhang, H. Wu, S. J. Pennycook and J. Wang, Metal–organic framework derived hollow CoS_2 nanotube arrays: an efficient bifunctional electrocatalyst for overall water splitting, *Nanoscale Horiz.*, 2017, **2**, 342-348.
20. S. Li, P. Ren, C. Yang, X. Liu, Z. Yin, W. Li, H. Yang, J. Li, X. Wang, Y. Wang, R. Cao, L. Lin, S. Yao, X. Wen and D. Ma, Fe_5C_2 nanoparticles as low-cost HER electrocatalyst: the importance of Co substitution, *Sci. Bull.*, 2018, **63**, 1358-1363.
21. Q. Wang, Z.-Y. Tian, W.-J. Cui, N. Hu, S.-M. Zhang, Y.-Y. Ma and Z.-G. Han, Hierarchical flower-like CoS2-MoS2 heterostructure spheres as efficient bifunctional electrocatalyst for overall water splitting, *Int. J. Hydrogen Energy*, 2022, **47**, 12629-12641.
22. Y.-J. Tang, A. M. Zhang, H.-J. Zhu, L.-Z. Dong, X.-L. Wang, S.-L. Li, M. Han, X.-X. Xu and Y.-Q. Lan, Polyoxometalate precursors for precisely controlled synthesis of bimetallic sulfide heterostructure through nucleation-doping competition, *Nanoscale*, 2018, **10**, 8404-8412.
23. X. Du, Y. Ding and X. Zhang, MOF-derived Zn–Co–Ni sulfides with hollow nanosword arrays for high-efficiency overall water and urea electrolysis, *Green Energy Environ.*, 2023, **8**, 798-811.
24. Y. Wang, Y. Pan, L. Zhu, H. Yu, B. Duan, R. Wang, Z. Zhang and S. Qiu, Solvent-free assembly of Co/Fe-containing MOFs derived N-doped mesoporous carbon nanosheets for ORR and HER, *Carbon*, 2019, **146**, 671-679.
25. Y. Gao, L. Qi, F. He, Y. Xue and Y. Li, Selectively Growing a Highly Active Interface of Mixed Nb–Rh Oxide/2D Carbon for Electrocatalytic Hydrogen Production, *Adv. Sci.*, 2022, **9**, 2104706.
26. X. H. Chen, X. L. Li, L. L. Wu, H. C. Fu, J. Luo, L. Shen, Q. Zhang, J. L. Lei, H. Q. Luo and N. B. Li, Nb_2O_5–Ni_3N heterojunction tuned by interface oxygen vacancy engineering for the enhancement of electrocatalytic hydrogen evolution activity, *J. Mater. Chem. A*, 2021, **9**, 11563-11570.
27. S. Zhao, C. Tan, C.-T. He, J. Dong and Z. Tang, Structural transformation of highly active metal-organic framework electrocatalysts during the oxygen evolution reaction, *Nat. Energy*, 2020, **5**, 881-890.